Supplementary information

Photoexcited triplet states of twisted acenes investigated by Electron Paramagnetic Resonance

Claudia E. Tait,*[a] Anjan Bedi,[b] Ori Gidron,[b] and Jan Behrends*[a]

S1 UV-vis spectra at room temperature and 80 K

UV-vis measurements at room temperature and 80 K were performed using a Varian Cary 100 Scan spectrometer with an Oxford Instruments nitrogen-cooled optical cryostat. The 50 μM solutions were filled into 3.9 mm OD, 3.0 mm ID quartz tubes and flash-frozen in liquid nitrogen before insertion into the cryostat for the low temperature measurements. Baseline-correction was performed with a reference sample containing pure toluene. The p-band region of the resulting spectra is shown in Figure S1, accurate measurement of the β-bands was prevented by the overlap with the toluene absorption peak.

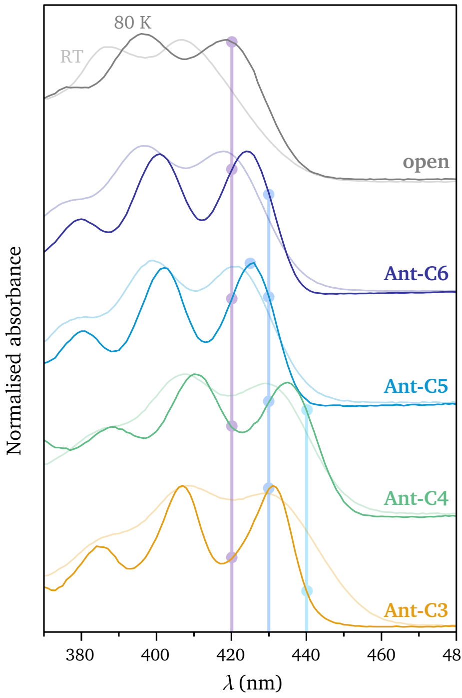

Fig. S1 UV-vis absorption spectra for **Ant-C*n*** (***n*** = 3-6) and the **open** reference compound recorded at room temperature and at 80 K. The excitation wavelengths used in the time-resolved EPR measurements are indicated by the vertical lines and coloured dots.

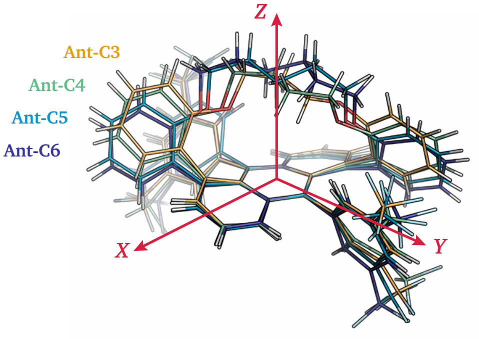

Fig. S2 Comparison of the crystal structures for **Ant-C*n*** (***n*** = 3-6).[1] The orientation of the ZFS tensor with respect to the molecules is also shown.

S2 Time-dependence of the triplet state EPR spectra

The evolution of the spectral shape as a function of time after laser excitation is depicted in Figure S4 for **Ant-C*n*** (***n*** = 3-6) and the **open** reference compound excited at 420 nm and for **Ant-C4** and **Ant-C3** excited at different wavelengths. A similar behaviour is observed for all compounds and excitation wavelengths: the initial spin polarisation is maintained throughout, however an increased broadening of the spectral features is observed after about 1 μs. The differences in ZFS parameters for the different compounds and for excitation at different wavelengths are still discernible within the whole measurement time window of 15 μs. No significant differences were observed in the decay behaviour at the canonical field positions for compounds with different twist angles, indicating similar triplet state lifetimes and relaxation behaviour.

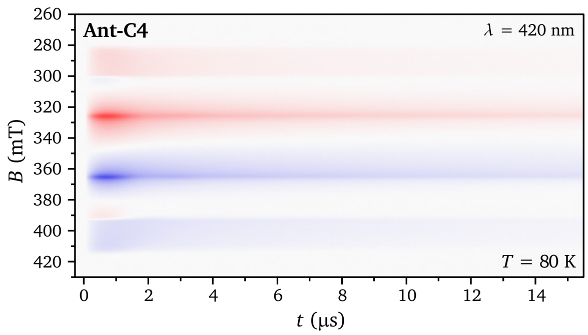

Fig. S3 Experimental transient EPR data for **Ant-C4** at 80 K after excitation at 420 nm (red - emissive, blue - absorptive).

---

[a] *Department of Physics, Freie Universität Berlin, Arnimallee 14, 14195 Berlin, Germany. E-mail: claudia.tait@fu-berlin.de, j.behrends@fu-berlin.de*

[b] *Institute of Chemistry, The Hebrew University of Jerusalem, Edmond J. Safra Campus, Jerusalem 91904, Israel.*

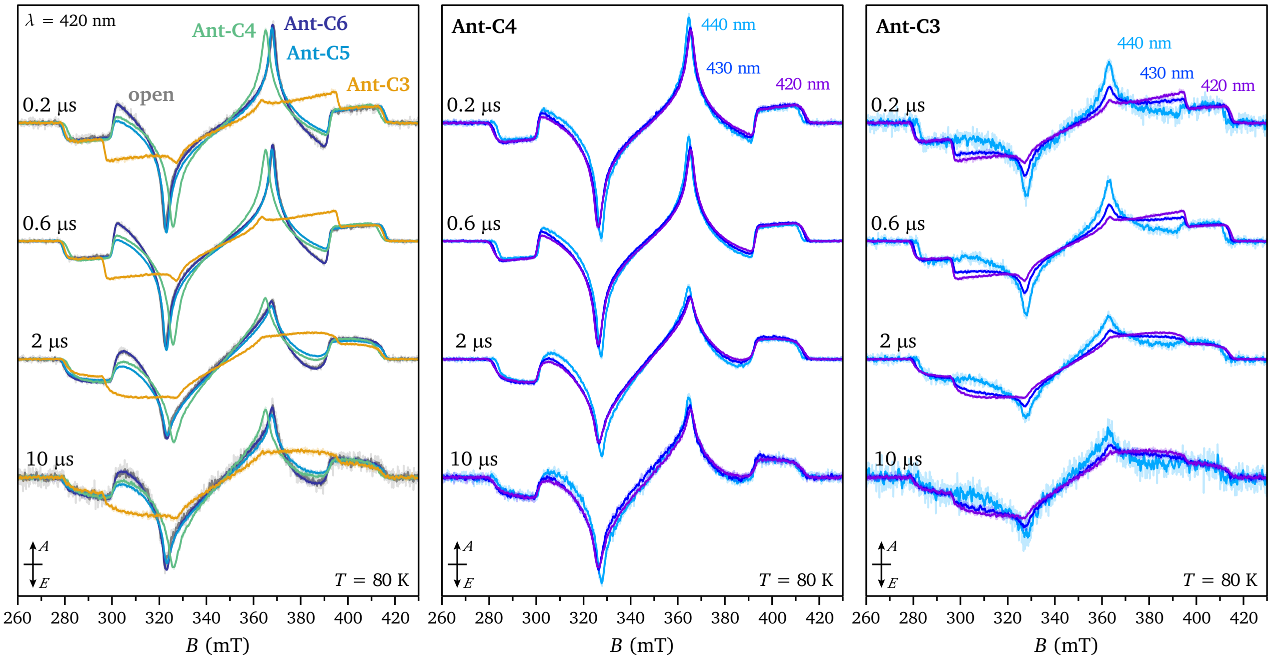

Fig. S4 Comparison of experimental transient EPR spectra at different times after the laser flash recorded with an excitation wavelength of 420 ns for **Ant-C*n*** (*n* = 3-6) and the **open** reference compound (*left*), for **Ant-C4** excited at different wavelengths (*middle*), and for **Ant-C3** excited at different wavelengths (*right*). All measurements were performed at 80 K. The displayed spectra are normalised by absolute signal area. For increased signal-to-noise the spectra were averaged over 0.2 μs, 0.2 μs, 0.5 μs (1 μs for **Ant-C3**), 2 μs (4 μs for **Ant-C3**), respectively (integration windows centred at the delay after flash indicated in the figure). No significant changes in spectral shape occur within these integration windows.

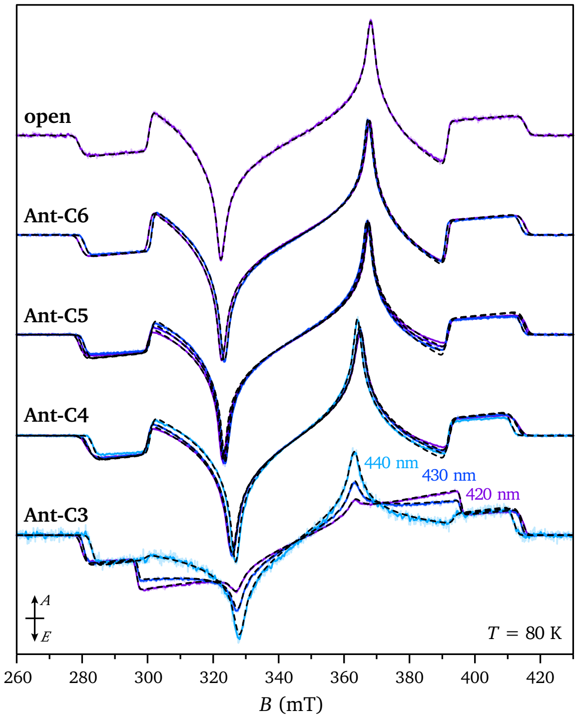

Fig. S5 Experimental transient EPR spectra of **Ant-C*n*** (*n* = 3-6) and the **open** reference compound recorded at short times after the laser flash (0.2 μs to 0.7 μs) at 80 K after excitation at different wavelengths compared to simulations (dashed black lines) performed with EasySpin[2] using the parameters reported in Table S1.

S3 Simulation of the triplet state EPR spectra

The EPR spectra extracted by integration over the range from 0.2 μs to 0.7 μs after the laser pulse were simulated using the EasySpin toolbox[2] in Matlab. In addition to the ZFS parameters D and E and the relative sublevel populations, line broadenings in the range of 50-100 MHz were used as additional fit parameters. The experimental spectra and simulations are shown in Figure S5 and the corresponding fit parameters are listed in Table S1.

Table S1 ZFS parameters and relative sublevel populations determined from simulations of the transient EPR spectra integrated from 0.2 μs to 0.7 μs after the laser flash. (The lowest sublevel population has been set to zero; the error on the relative populations corresponds to 0.005-0.010.)

	λ (nm)	D (MHz)	E (MHz)	p_X	p_Y	p_Z
open	420	1910 ± 2	-211 ± 1	0.000	0.994	0.006
Ant-C6	420	1904 ± 1	-215 ± 1	0.000	0.999	0.001
	430	1865 ± 1	-213 ± 1	0.000	0.989	0.011
Ant-C5	420	1905 ± 3	-220 ± 1	0.131	0.869	0.000
	425	1889 ± 3	-220 ± 1	0.095	0.905	0.000
	430	1868 ± 3	-220 ± 1	0.062	0.938	0.000
Ant-C4	420	1838 ± 3	-248 ± 1	0.087	0.913	0.000
	430	1830 ± 2	-248 ± 1	0.063	0.937	0.000
	440	1791 ± 4	-250 ± 1	0.016	0.984	0.000
Ant-C3	420	1890 ± 3	-294 ± 2	0.539	0.461	0.000
	430	1870 ± 3	-293 ± 2	0.445	0.555	0.000
	440	1804 ± 8	-275 ± 3	0.280	0.720	0.000

S4 Additional ENDOR figures

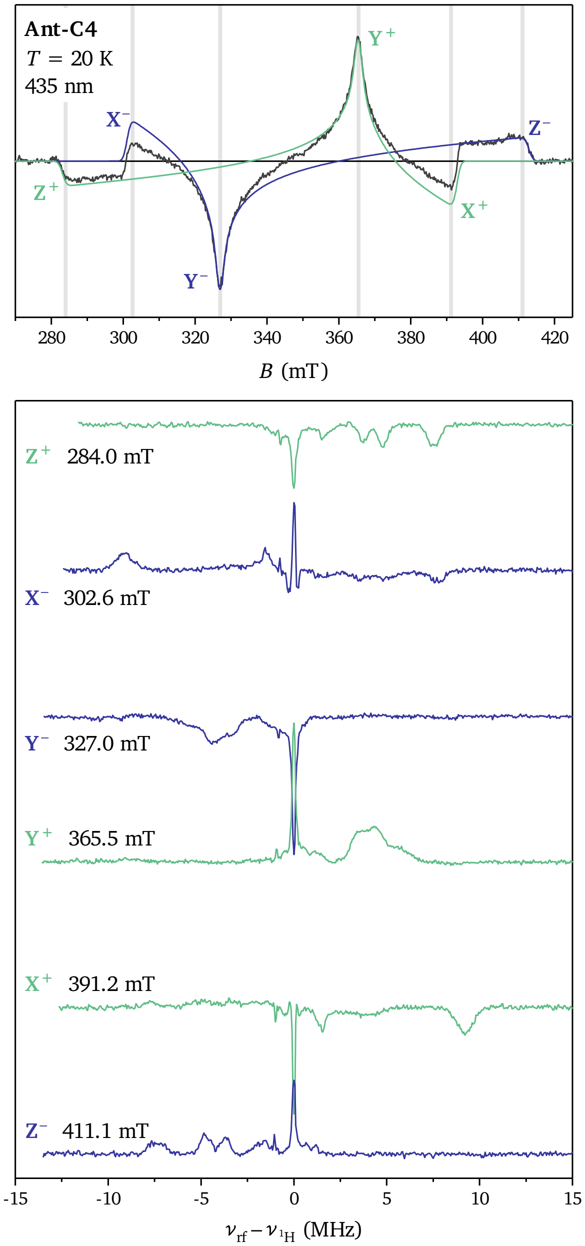

Fig. S6 (*top*) Field-swept echo-detected EPR spectrum recorded for **Ant-C4** and (*bottom*) Davies ENDOR spectra recorded at the six canonical field positions indicated by grey lines in the spectrum.

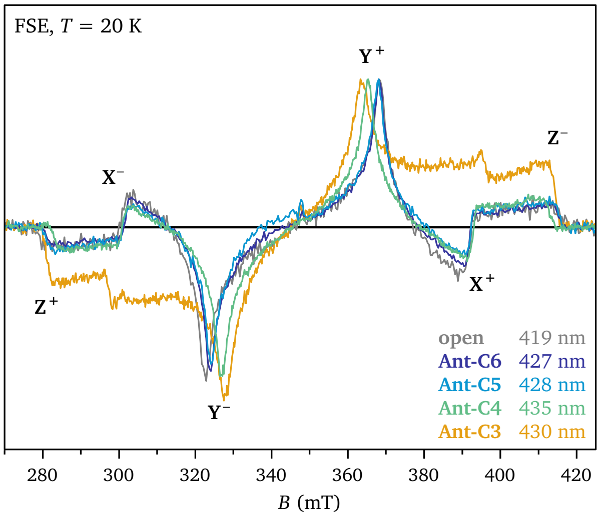

Fig. S7 Field-swept echo-detected EPR spectra recorded for **Ant-C*n*** (*n* = 3-6) and the **open** reference compound for the excitation wavelengths used for the ENDOR measurements. The ENDOR measurements were performed at the three high-field canonical positions.

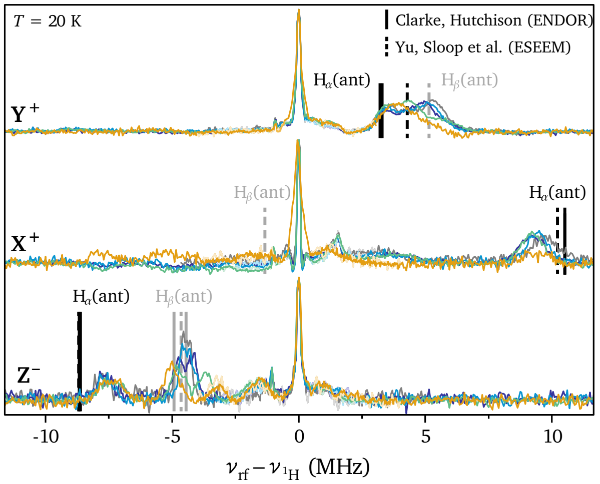

Fig. S8 ENDOR spectra recorded at the high field canonical field positions for **Ant-C*n*** (*n* = 3-6) and the **open** reference compound (T = 20 K, excitation wavelengths: **open** 419 nm, **Ant-C6** 427 nm, **Ant-C5** 428 nm, **Ant-C4** 435 nm, **Ant-C3** 430 nm. The vertical lines correspond to the hyperfine couplings of the α and β protons determined for the photoexcited triplet state of anthracene reported by Clarke and Hutchison[3] and by Yu *et al.*[4].

S5 Modelling of the experimental ENDOR data

DFT calculations on the triplet states of the **open** reference compound and the **Ant-C*n*** series with n = 3-6 were performed in ORCA[5,6] using the PBE0 functional and the EPRII basis set.[7] The hyperfine coupling values were calculated both for ground-state optimised geometries as well as geometries optimised in the triplet state at the BP86/def2-SVP or PBE0/def2-TZVP level including the atom-pairwise dispersion correction using the Becke-Johnson damping scheme.[8,9] The best agreement with the experimental data was obtained for the ground-state geometries reported by Bedi *et al.*[1] and the corresponding twist angles are in good agreement with the values determined from the crystal structures of the **Ant-C*n*** compounds. DFT predicts similar twist angles for the **open** compound and for **Ant-C6** (21.2° and 21.1°, respectively). A calculation of the ZFS parameters by DFT was attempted, however the D values were underestimated for a factor of about 2 and the calculated E values were significantly smaller than those observed experimentally. DFT does however reproduce the qualitative trend of decreasing D values for increasing twist angles. In addition to the significant deviation between the magnitude of the ZFS parameters, the in-plane orientations of the ZFS tensors resulting from the DFT calculations for **Ant-C*n*** deviate significantly from the known orientations of the in-plane axes in anthracene and are also predicted to rotate as a function of twist angle. Such a reorientation of the ZFS tensor is clearly at odds with the experimental ENDOR results, which are in agreement with the same orientation of the ZFS tensor with respect to the acene core as in anthracene. In all of the modelling and interpretation of the experimental data the ZFS tensor orientation in the molecular frame was therefore assumed to be as determined for the series of linear acenes:[3] the X axis corresponds to the long in-plane axis, Y to the short in-plane axis and Z to the out-of-plane axis (see Figure 1 in the main text). The failure of DFT in estimating the ZFS parameters of aromatic organic molecules, including acenes, is relatively well known[10] and CASSCF calculations, including static π-electron correlation, would likely yield a closer agreement with the experimental results.

The triplet state ENDOR spectra modelled on the basis of the proton hyperfine couplings determined by DFT are compared to the experimental data in the left panel of Figure S10. The ENDOR spectra were constructed as a sum of Gaussians centred at hyperfine values corresponding to the projection of the calculated HFI tensors onto the ZFS tensor axes. The width of the Gaussians was adjusted to match the experimental data. The resulting spectra were multiplied by the Davies ENDOR intensity function determined by length of the inversion π pulse. The agreement with the experimental data is reasonable, implying that the computed spin density distribution reproduces the experimental one relatively well. The largest deviations are observed for the ENDOR peaks assigned to the H_α and H_β protons directly bound to the acene core. The calculated hyperfine couplings, especially as regards the out-of-plane contribution of the H_β protons, were found to be strongly dependent on the exact molecular geometry, which might not reflect the actual geometry of the molecules in toluene solution. Additionally, potential energy surface scans performed by DFT predict that a range of twist angles and a range of relative orientations of phenyl side groups are accessible, therefore likely leading to a distribution of ZFS and hyperfine values.

In order to gain more insight into the correlation between the changes in hyperfine couplings and the changes in geometry induced by shortening of the diagonal tether in **Ant-C*n*** a simpler modelling approach was pursued. As described in the main text, the change in geometry introduced by twisting the anthracene core, even in the absence of changes in the spin density distribution, would already lead to changes in the hyperfine couplings probed by orientation-selective ENDOR experiments performed at field positions corresponding to the canonical orientations of the ZFS tensor. The extent of these changes was modelled for H_α and H_β by computing the predicted orientations of the HFI tensors of these protons based on the local geometry of the C-H bond and the surrounding aromatic carbon nuclei in the crystal structures. The principal components of the hyperfine coupling tensors were optimised for the **open** compound using the DFT values and the literature values for anthracene[3,4] as starting values. The same principal components were used for the **Ant-C*n*** series and the tensor orientations were adapted based on the corresponding geometries. The ENDOR spectra were then constructed as described above for the DFT-predicted hyperfine tensors, however only the H_α and the two types of H_β protons were considered. The resulting spectra are compared to the experimental data in the central panel of Figure S10 (Model A). The comparison shows that the change in geometry accounts for the decrease in the H_α hyperfine value detected along the out-of-plane axis of the ZFS tensor, but does not quite account for the remaining changes with increasing twist angle, in particular the splitting of the H_β peak observed in the spectrum recorded at the Z^- field position into two components for the compounds with the highest twist angles.

The right panel in Figure S10 (Model B) shows the result of least-squares fitting of the principal components of the H_α, H_{β_1} and H_{β_2} hyperfine tensors to the experimental data. The resulting values are listed in Table S2. The changes required for the H_α hyperfine tensor are relatively small, as large part of the changes observed in the corresponding hyperfine peaks is due to the change in relative orientation of the HFI and ZFS tensors induced by increased twisting. More significant changes are required for the H_β protons, suggesting a redistribution of the spin density, likely towards the phenyl groups attached to the anthracene core close to the H_{β_2} proton.

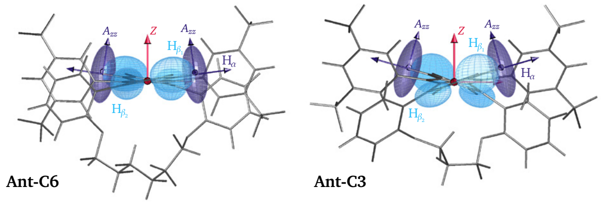

Fig. S9 Hyperfine tensors and principal axes displayed with respect to the molecular geometry for **Ant-C6** and **Ant-C3** and with respect to the Z axis of the ZFS tensor.

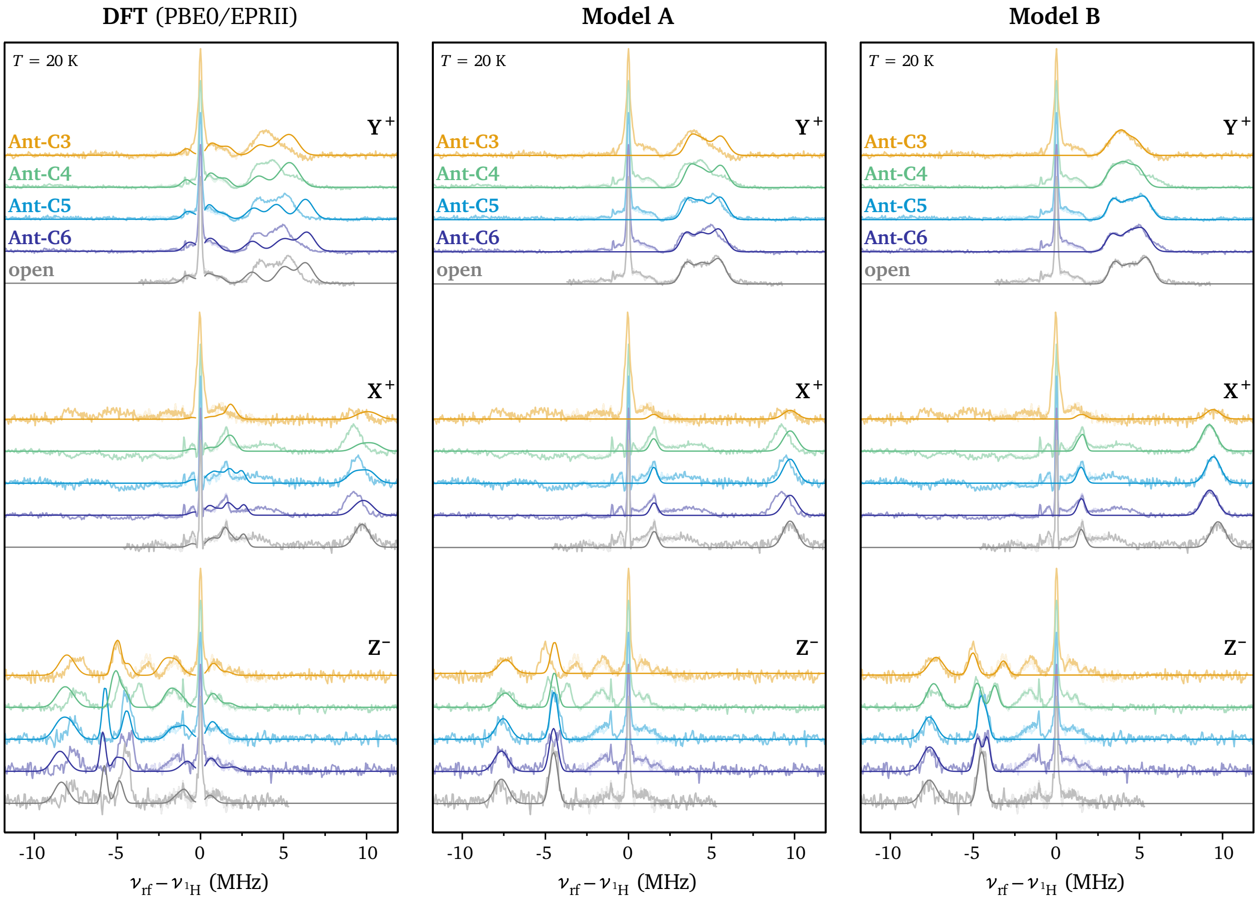

Fig. S10 Comparison of modelled ENDOR spectra with the experimental data recorded for **Ant-C*n*** (*n* = 3-6) and the **open** reference compound. In all cases the modelled ENDOR spectra are constructed as a sum of Gaussians considering the hyperfine coupling value along the corresponding canonical orientation. The DFT model is based on the tensor orientations and principal components from DFT calculations performed at the PBE0/EPRII level on the triplet state using the ground-state-optimised geometry. For models A and B, only the protons H_α, H_{β_1} and H_{β_2} are considered with tensor orientations determined based on the geometry of the anthracene core. The principal values for model A are selected to match the experimental data for **open**, while for model B, the individual principal components are optimised individually for each of the compounds. The principal components of the hyperfine coupling tensors used in the calculations are listed in Table S2.

Table S2 Principal values in MHz of the hyperfine tensors of the α, β_1 and β_2 protons on the anthracene core as predicted by DFT at PBE0/EPRII level and as used in the modelling of the ENDOR data. (The uncertainty in the principal values of the hyperfine tensors determined in Models A and B is estimated to be in the range from 0.05-0.10 MHz.)

			H_α			H_{β_1}			H_{β_2}	
		A_{xx}	A_{yy}	A_{zz}	A_{xx}	A_{yy}	A_{zz}	A_{xx}	A_{yy}	A_{zz}
open	DFT	-2.90	-9.72	-8.50	-1.10	-7.67	-5.87	-0.44	-6.05	-4.83
	Model A	-3.35	-9.73	-7.70	0.53	-7.45	-4.47	-0.27	-5.50	-4.6
	Model B	-3.35	-9.73	-7.70	0.53	-7.45	-4.47	-0.27	-5.50	-4.60
Ant-C6	DFT	-2.93	-9.79	-8.56	-1.12	-7.77	-5.95	-0.34	-6.03	-4.80
	Model A	-3.35	-9.73	-7.70	0.53	-7.45	-4.47	-0.27	-5.50	-4.6
	Model B	-3.21	-9.22	-7.68	0.49	-7.09	-4.83	-0.24	-5.45	-4.15
Ant-C5	DFT	-2.81	-9.71	-8.47	-1.08	-7.59	-5.82	0.07	-5.67	-4.37
	Model A	-3.35	-9.73	-7.70	0.53	-7.45	-4.47	-0.27	-5.50	-4.6
	Model B	-3.15	-9.43	-7.82	0.59	-7.10	-4.69	-0.33	-5.42	-4.28
Ant-C4	DFT	-2.93	-10.04	-8.62	-0.80	-6.66	-5.23	-0.11	-6.26	-4.66
	Model A	-3.35	-9.73	-7.70	0.53	-7.45	-4.47	-0.27	-5.50	-4.6
	Model B	-2.95	-9.18	-7.69	0.31	-6.31	-4.88	-0.49	-5.04	-3.77
Ant-C3	DFT	-2.92	-10.05	-8.61	-0.73	-6.42	-5.08	-0.08	-6.31	-4.66
	Model A	-3.35	-9.73	-7.70	0.53	-7.45	-4.47	-0.27	-5.50	-4.6
	Model B	-2.90	-9.41	-7.59	0.13	-5.92	-5.16	-0.49	-5.00	-3.21

References

1 A. Bedi, L. J. W. Shimon and O. Gidron, *J. Am. Chem. Soc.*, 2018, **140**, 8086–8090.

2 S. Stoll and A. Schweiger, *J. Magn. Reson.*, 2006, **178**, 42–55.

3 R. H. Clarke and C. A. Hutchison, *J. Chem. Phys.*, 1971, **54**, 2962–2968.

4 H. L. Yu, D. J. Sloop, S. I. Weissman, T.-S. Lin, J. R. Norris and M. K. Bowman, *J. Phys. Chem.*, 1982, **86**, 4287–4290.

5 F. Neese, *WIRES: Comput. Mol. Sci.*, 2012, **2**, 73–78.

6 F. Neese, *WIRES: Comput. Mol. Sci.*, 2018, **8**, e1327–1–6.

7 V. Barone, *Recent Advances in Density Functional Methods*, World Scientific Publ. Co., Singapore, 1995, vol. 1, ch. 8, pp. 287–334.

8 S. Grimme, J. Antony, S. Ehrlich and H. Krieg, *J. Chem. Phys.*, 2010, **132**, 154104–1–19.

9 S. Grimme, S. Ehrlich and L. Goerigk, *J. Comput. Chem.*, 2011, **32**, 1456–1465.

10 S. Sinnecker and F. Neese, *J. Phys. Chem. A*, 2006, **110**, 12267–12275.